Finite-difference solution of the eikonal equation for transversely isotropic media

David W.S. Eaton

ABSTRACT

A new finite-difference technique is presented for solving the eikonal equation for inhomogeneous, transversely isotropic media. The method is an extension of other recently developed, isotropic finite-difference algorithms. An expanding-wavefront scheme on a triangular mesh of points is employed, in order to ensure causality and minimize grid anisotropy. Several examples are presented to illustrate the method for varying degrees of anisotropy and inhomogeneity. This technique is particularly well suited to tomographic and migration/inversion applications, since the traveltimes can be efficiently calculated on a dense grid of points for a smoothly varying background.

INTRODUCTION

The calculation of seismic traveltimes is a fundamental problem in exploration seismology, with applications in forward modeling, tomography, migration and inversion. For inhomogeneous and/or anisotropic media, the calculation of traveltimes is difficult and often time consuming. This study presents a new algorithm that employs a finite difference approach to calculate the traveltime function, τ, for qP and qS waves in inhomogeneous, transversely isotropic media.

In the high-frequency approximation, the traveltime function is governed by the eikonal equation (Bleistein, 1986). The traditional approach to solving for τ involves some form of iterative ray tracing. Mathematically, this approach corresponds to solution of the eikonal equation by the method of characteristics (see Musgrave, 1970; Bleistein, 1986). For applications that require traveltimes on a grid of points, interpolation of the ray-traced traveltimes is essential. Because of its iterative nature, ray tracing through complex models can be expensive and cumbersome.

Solution of the eikonal equation using finite differences was proposed recently by Vidale (1988). Here the wavefronts, rather than traditional rays, are tracked. A major advantage of this method is that the data are directly calculated onto a grid of points; no subsequent interpolation is required. However, the traveltime function is constrained to be single-valued; thus this technique is well suited to modeling first-arrival traveltimes. Vidale (1988) demonstrated that this method correctly treats head waves, and shadow zones are filled with the appropriate diffractions. Qin et al. (1990) have modified Vidale's algorithm by employing an expanding wavefront technique in order to honour the principle of causality.

Here, the method of Qin et al. (1990) is modified further using a triangular mesh of points (Figure 1) similar to grids employed to model fluid flow using cellular automata (eg. Rothman, 1988). This modification lends additional symmetry

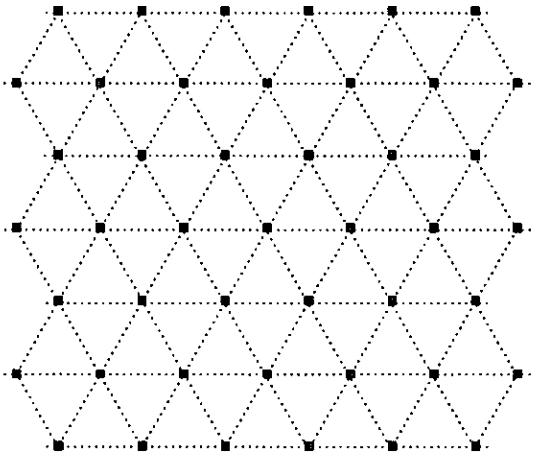

FIG. 1. Triangular grid used for finite-difference algorithm. Each point is surrounded by six nearest neighbours in a hexagonal configuration.

to the finite-difference operator, reduces grid anisotropy, and facilitates the extension of the technique to include anisotropic (in this case, transversely isotropic) media.

In an exploration context, the principle causes of transverse isotropy are parallel alignment of elongated mineral grains in clays and shales, periodic thin layering and preferred alignment of cracks (Crampin et al., 1984). Incorporation of anisotropy into the modeling procedure leads to complications, such as cusps and triplications in the wave surface, that stem from the difference in magnitude and direction between the group and phase velocities. Preliminary results appear to indicate that the method considered here is suitable only for modeling weak anisotropy. However, measurements made for sedimentary rocks indicate that strong anisotropy is uncommon (Thomsen, 1986).

BACKGROUND THEORY

The eikonal equation in two dimensions (corresponding to the scalar wave equation) can be written

$$\left(\frac{\partial \tau}{\partial x}\right)^2 + \left(\frac{\partial \tau}{\partial z}\right)^2 = p(x,z)^2 \quad , \tag{1}$$

where p is slowness and the traveltime function, τ, is constant along a wavefront surface. Equation (1) is then simply an expression for the magnitude of the slowness vector, $\mathbf{p} = \nabla\tau$. The components of $\mathbf{p}$ need not be measured in the x- and z-directions, but must be mutually orthogonal. Referring to Figure 2, a second-order

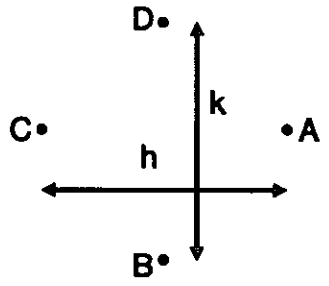

FIG. 2. Basic cell of 4 points for finite difference calculation.

finite-difference approximation to (1) at the centroid of four points (comprising a *cell*) may be written

$$\left(\frac{\tau_A - \tau_C}{h}\right)^2 + \left(\frac{\tau_B - \tau_D}{k}\right)^2 = p^2 \quad . \tag{2}$$

If the traveltimes for three out of four points are known, the fourth traveltime (eg. τ_A) can be solved for using the quadratic formula,

$$\tau_A = \tau_C + \sqrt{h^2 p^2 - (h/k)(\tau_B - \tau_C)^2} \quad . \tag{3}$$

Equation (3) is the same as previous isotropic finite-difference formulae for a square grid when $h = k = \sqrt{2}\Delta x$, where Δx is the grid interval.

The differential equation governing τ in anisotropic elastic media is somewhat more complex, and has the form (see Appendix)

$$det\left|\tau_{,i}\tau_{,l}c_{ijkl} - \rho\delta_{jk}\right| = 0 \ , \tag{4}$$

where Einstein's summation notation is employed, a comma implies spatial differentiation, δ_{jk} is the Kronecker delta and c_{ijkl} is the tensor of elastic stiffnesses. Multiplying (4) by the phase velocity squared (v^2) gives the Kelvin-Christoffel equation

$$det\left|\Gamma_{jk} - \rho v^2\delta_{jk}\right| = 0 \ , \tag{5}$$

where $\Gamma_{jk} = n_i n_l c_{ijkl}$ and n_i is the unit vector normal to the wavefront. Thus, if the direction of propagation and the type of wave (eg. *qP*, *qS1*, *qS2*) is known, the magnitude of the slowness vector (ie. $1/v^2$) can be computed using (5). A finite-difference algorithm similar to previous isotropic algorithms can then be implemented by estimating a direction for the wavefront normal, solving for the magnitude of the phase slowness, and then updating the traveltime using (3). This approach avoids the finite-difference approximation to equation (4) and the necessity to solve a sixth-order polynomial equation.

For transversely isotropic media, analytic solutions to (5) exist in several forms. Using the parameterization suggested by Thomsen (1986), the phase velocities may be written

$$v_P(\theta) = \alpha_0\left[1 + \varepsilon\sin^2\theta + D^*(\theta)\right]^{1/2} \quad , \tag{6}$$

$$v_{SV}(\theta) = \beta_0\left[1 + (\alpha_0/\beta_0)^2\varepsilon\sin^2\theta - (\alpha_0/\beta_0)^2 D^*(\theta)\right]^{1/2} \quad , \tag{7}$$

$$v_{SH}(\theta) = \beta_0\left[1 + 2\gamma\sin^2\theta\right]^{1/2} \quad , \tag{8}$$

with

$$D^*(\theta) \equiv (1/2)\xi\left\{\left[1 + 4(\delta^*/\xi)\sin^2\theta\cos^2\theta + 4(\xi+\varepsilon)(\varepsilon/\xi)\sin^4\theta\right]^{1/2} - 1\right\} \quad , \tag{9}$$

and

$$\xi = 1 - (\beta_0/\alpha_0)^2 \quad . \tag{10}$$

Here θ is the angle that the wavefront normal subtends with the axis of symmetry, α_0 and β_0 are the *qP*- and *qS*-wave velocities in the direction of the symmetry axis, and ε, δ and γ are anisotropy parameters that vanish for isotropic media. These parameters can be defined in terms of elastic stiffnesses as follows (Thomsen, 1986):

$$\alpha_0 \equiv \sqrt{C_{33}/\rho} \quad , \tag{11}$$

$$\beta_0 \equiv \sqrt{C_{44}/\rho} \quad , \tag{12}$$

$$\varepsilon \equiv (C_{11}-C_{33})/(2C_{33}) \quad , \tag{13}$$

$$\gamma \equiv (C_{66}-C_{44})/(2C_{44}) \quad , \tag{14}$$

and

$$\delta \equiv \frac{(C_{13} + C_{44})^2 - (C_{33} - C_{44})^2}{2C_{33}(C_{33} - C_{44})} \quad . \tag{15}$$

The parameter δ^* is defined

$$\delta^* \equiv (2\delta - \varepsilon)\xi \quad . \tag{16}$$

Using these formulas for phase velocity, an algorithm is described below for solving for the traveltime, τ, in transversely isotropic media.

DESCRIPTION OF THE ALGORITHM

The algorithm used here is an adaptation from the work of Qin et al. (1990) and Vidale (1988). However, a triangular grid is employed rather than a square grid, for

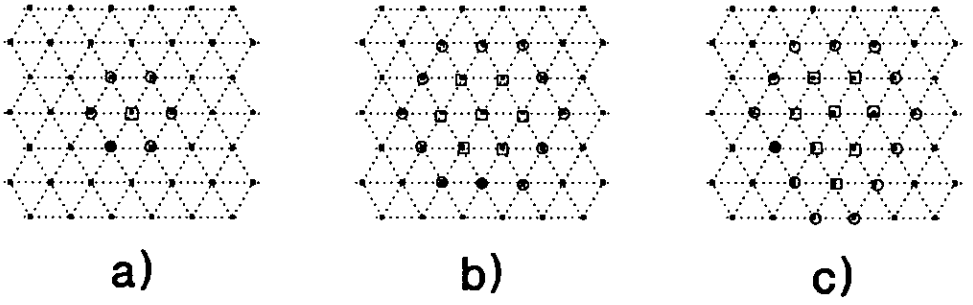

FIG. 3. a) The first step in the algorithm is the calculation of times for the six neighbouring points around source point (square). The current wavefront is represented by circles. The solid circle indicates the point with the minimum τ on the current wavefront. b) Timed points after several more iterations. Squares represent points that are timed, but not on the current wavefront. c) Timed points one iteration after c).

reasons that are discussed below. The first step is the calculation of the traveltimes for the six points surrounding the source point (Figure 3a). The traveltime at each point can be calculated using

$$\tau_i = \tau_0 + h \cdot p \tag{17}$$

where p is the phase slowness calculated using the averaged elastic parameters between the source point and the point being updated, and τ_0 is the time at the source grid point (normally zero). The six points surrounding the source now make up the current wavefront. A separate logical array is used to identify those points that lie on the current wavefront. Further updates always proceed from the global minimum on the current wavefront, to ensure causality (ie. any point that is about to be timed will have had all of the points along the associated raypath already timed, see Qin et al., 1990). All legal neighbouring points around the current minimum that have not been timed are updated using equation (3), with the slowness calculated using average medium parameters at the centroid. If more then one method of updating a particular point exists, all are calculated and the minimum is used.

It is useful at this point to clarify the description with a number of definitions. The current wavefront is taken to be all points in the grid that have been timed, but are not completely surrounded by timed points (circles in Figure 3). This set of points will roughly approximate the true wavefront at any given iteration. Once all neighbouring points have been timed, a grid point is no longer active (squares in Figure 3). A legal point to be timed is one for which at least two neighbouring points are already timed. If only two neighbouring points have been timed, an alternative cell configuration is used (Figure 4b).

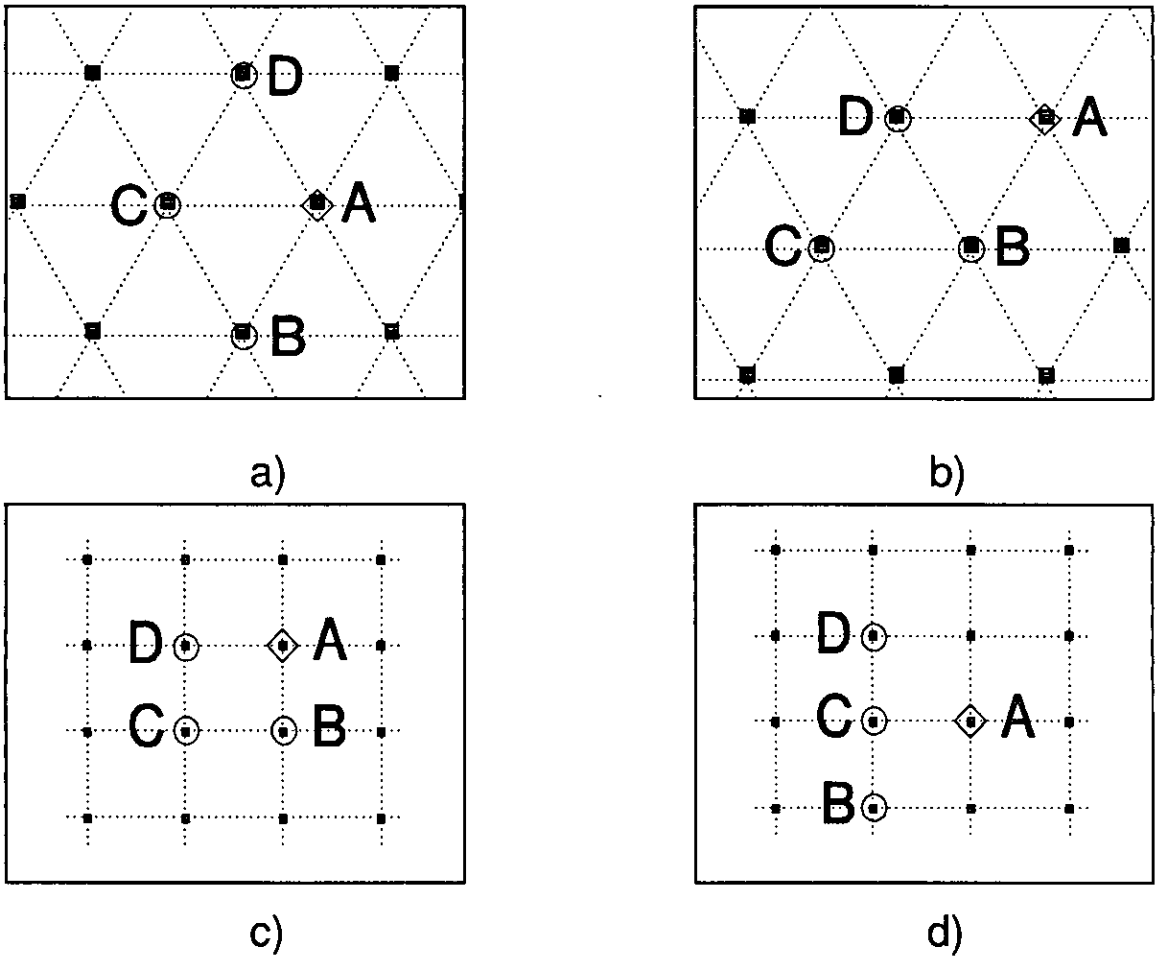

FIG. 4. a) Most common cell configuration for triangular grid. The point to be calculated (A) is indicated by a diamond. b) Alternative cell configuration for triangular grid. c) Most common cell configuration for square grid. d) Alternative cell configuration for square grid. Note that corresponding finite-difference operator is O(h) in the direction CA.

In order to calculate the slowness for an anisotropic medium, it is necessary to know the direction of the wavefront normal. Taking points B and D in the timing cell, it is possible to approximate the wavefront locally, assuming that the wave is planar. The direction of propagation for a plane wave that satisfies the times τ_B and τ_C is then determined in an iterative fashion. Some error, however, will occur for nonplanar wavefronts.

There are certain advantages of using a triangular grid rather than a square grid. In the latter case, it is sometimes necessary to update away from the wavefront using a T-shaped configuration (Figure 4d), which leads to a finite-difference operator that is only first-order accurate in the approximate direction of propagation

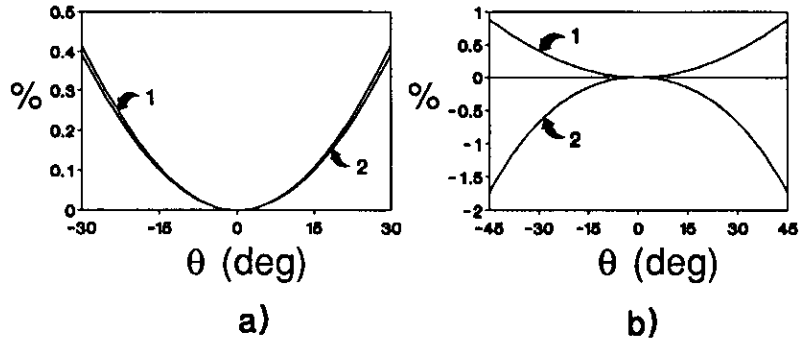

FIG. 5. a) Percentage error of finite-difference operator for a traingular grid. θ is the angle that the wavefront normal makes with the cell exis, CA, and lies in the range -30°≤θ≤30°. The radius of curvature of the wavefront is 2 grid units. 1 = most common cell configuration, 2 = alternative cell configuration (see Figure 4). b) Same as a), but for square grid. Note that -45°≤θ≤45°. 1 = most common cell configuration, 2 = alternative cell configuration.

(Vidale, 1988). For the case of a triangular grid, it is always possible to use a finite-difference operator that is $O(h^2)$. Furthermore, a certain degree of error is associated with the finite difference operator when the radius of curvature of the wavefront is small (Vidale, 1988). Since the degree of error varies with direction, this property is referred to here as *grid anisotropy*. Figure 5 shows error versus propagation direction for both the square and triangular grids, for a wavefront with radius of curvature equal to 2 grid units. The maximum error for the triangular grid is 0.4%, whereas the maximum error for the square grid is 1.7%. In both cases, the grid anisotropy becomes insignificant when the wavefront is nearly planar.

The program written to test this algorithm is still at a development stage. In the next section, three heuristic examples are presented. The model for the first example is isotropic and has two layers. The source is positioned in the low velocity layer, and the example illustrates how the algorithm is capable of modeling head waves. The second example is for a homogeneous, transversely isotropic medium, and is intended to show the limitations of this algorithm for modeling anisotropy. The third example models an antiformal structure containing an anisotropic zone.

EXAMPLES

The velocity model for the first example is illustrated in Figure 6. The source is located in a layer with velocity 3000 m/s, beneath a layer with velocity 5000 m/s. The entire calculated τ array, containing 12744 points, is displayed in Figure 7. Wavefronts, or surfaces of constant traveltime, are represented by the boundaries between different shades in Figure 7. Moving outward from the source point, snapshots of the wavefront at different times can be discerned. It is evident that

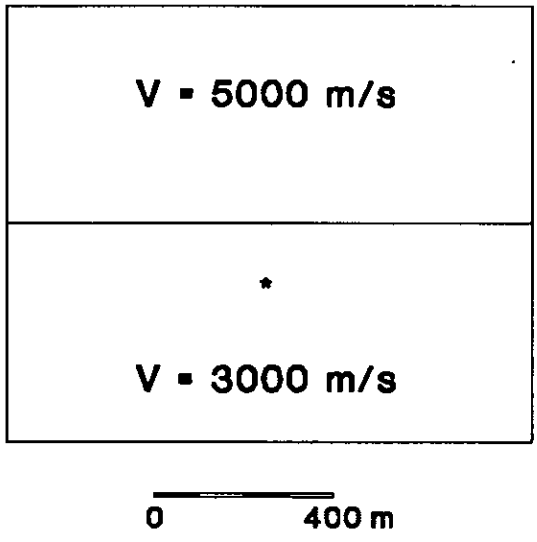

Fig. 6. Velocity model for example 1. Asterisk marks position of source.

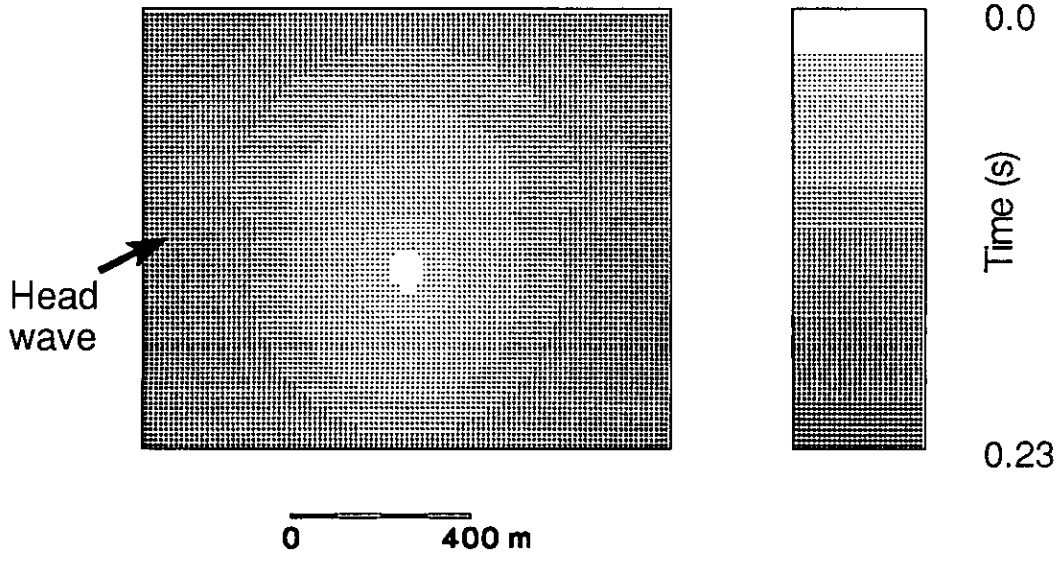

Fig. 7. Traveltime function, τ, calculated for example 1. Note head wave along interface.

after a certain time, when the corresponding ray has reached the critical angle, a head wave is generated along the interface.

Figure 8 shows subsets of the τ array, for a string of receivers at the top and bottom of the grid, as well as an array of receivers along the side of the grid (corresponding to a cross hole geometry). The part of the first arrival corresponding to the head wave is clearly evident in the cross-hole example (Figure 8b).

The second example shows the performance of the program for a homogeneous transversely isotropic medium. The parameters chosen correspond to measured values for the Pierre shale (White et al., 1982), a weakly anisotropic material, and are summarized in Table 1. The slowness surface, consisting of a *qP* and two *qS* sheets (approximately polarized in the SV and SH senses), were calculated using equations 6-8. One quadrant of a cross section through the slowness surface is illustrated in Figure 9a. The wave surface (or group velocity surface) is generated from the slowness surface, and represents the theoretical wavefronts at τ = 1s. Components of the group velocity, V_i, were calculated using (Kendall and Thomson, 1988)

$$V_i = \frac{c_{ijkl} p_l D_{jk}}{\rho D_{qq}} \quad , \tag{18}$$

where D_{jk} is a cofactor of the matrix $c_{ijkl} p_i p_l / \rho - \delta_{jk}$. Note that the *qP* and *qSH* wavefronts are nearly elliptical, whereas the *qSV* wavefront is nearly circular.

Anistropic parameters for a more strongly anisotropic medium are also shown in Table 1, corresponding to a shale under in situ conditions at a depth of about 1500 m in the Williston basin (Jones and Wang, 1981). The calculated slowness and wave surfaces for this shale are illustrated in Figure 10. By the principle of duality, points of inflection for the *qSV* slowness sheet in Figure 10a map to cusps in the wave surface in Figure 10b (Singh and Chapman, 1988). Thus the expanding *qSV* wave will produce three arrivals at some receiver locations. The waveform for arrivals on the reverse branch of the wave surface (AB in Figure 10b) is the Hilbert transform of the waveform for the forward branches of the wave surface (Singh and Chapman, 1988). Based on these observations for a relatively simple example of anisotropy, it is clear that wave propagation in anisotropic media is considerably more complex than for isotropic media.

The calculated τ arrays for the weakly anisotropic example are shown in Figure 11. The algorithm has correctly produced semi-elliptical wavefronts for *qP* and *qSH* propagation, but nearly circular wavefronts for *qSV* propagation. However, an artifact of the procedure is a noticeable tendency for the wavefronts to assume a hexagonal shape. This is almost certainly a consequence of the grid geometry, and is probably a result of systematic error in estimation of the direction of the wavefront normal for curved wavefronts. If so, it is possible that this artifact can be corrected for.

The program was successful in generating a τ array for *qP* propagation for the second shale, but not *qS* propagation. Possible reasons for the failure of the program for the second shale are:

1) the algorithm is most accurate when the wavefront can locally be well approximated by a plane wave. Hence, instabilities probably occur in the neighbourhood of cusps in the *qSV* wavefront (see Figure 10b);

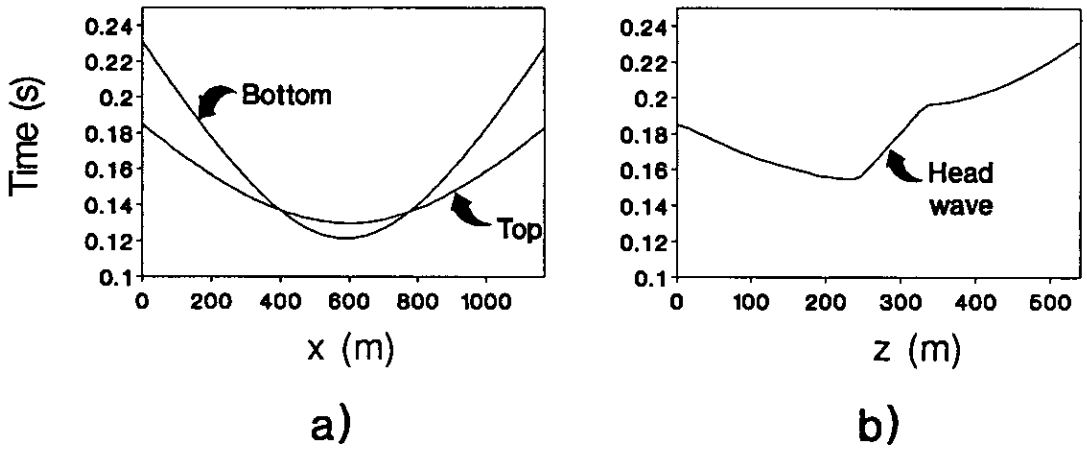

Fig. 8. a) Traveltimes at top and bottom of the grid for example 1. Only direct arrivals have been calculated. b) Traveltimes at side of grid, corresponding to a cross-hole geometry. In this case some of the first arrivals are from the head wave, rather than direct arrivals.

Anisotropic Parameters

	α_0 (m/s)	β_0 (m/s)	ε	δ	γ	ρ (kg/m^3)
1. Pierre shale	2074	869	0.110	0.090	0.165	2250
2. Williston basin shale	3377	1490	0.200	-0.075	0.510	2420

Table 1. Anisotropic parameters for Pierre shale (White et al., 1982) and Williston basin shale (Jones and Wang, 1981). See also Thomson (1986).

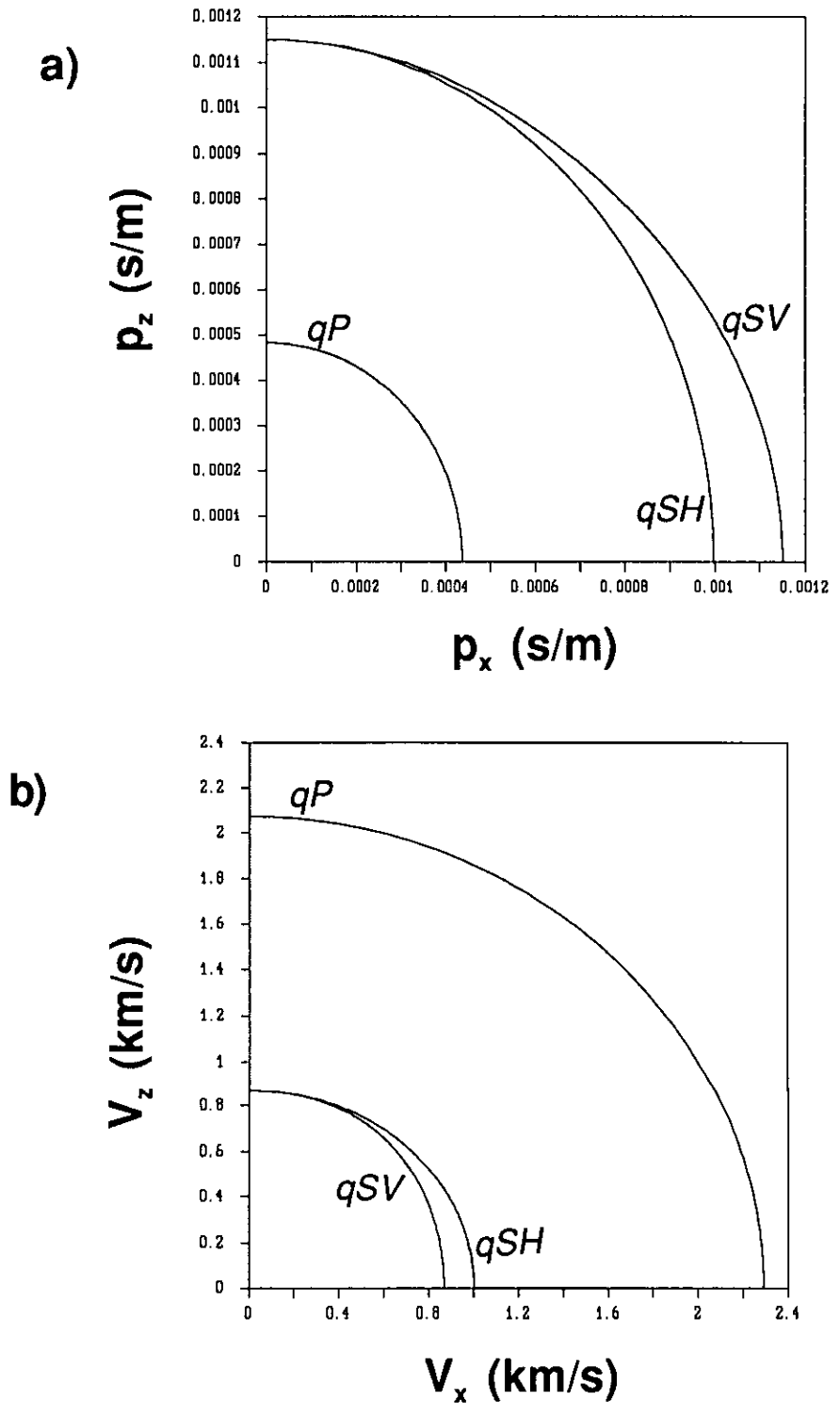

Fig. 9. a) Slowness surface for Pierre shale. b) Wave surface for Pierre shale.

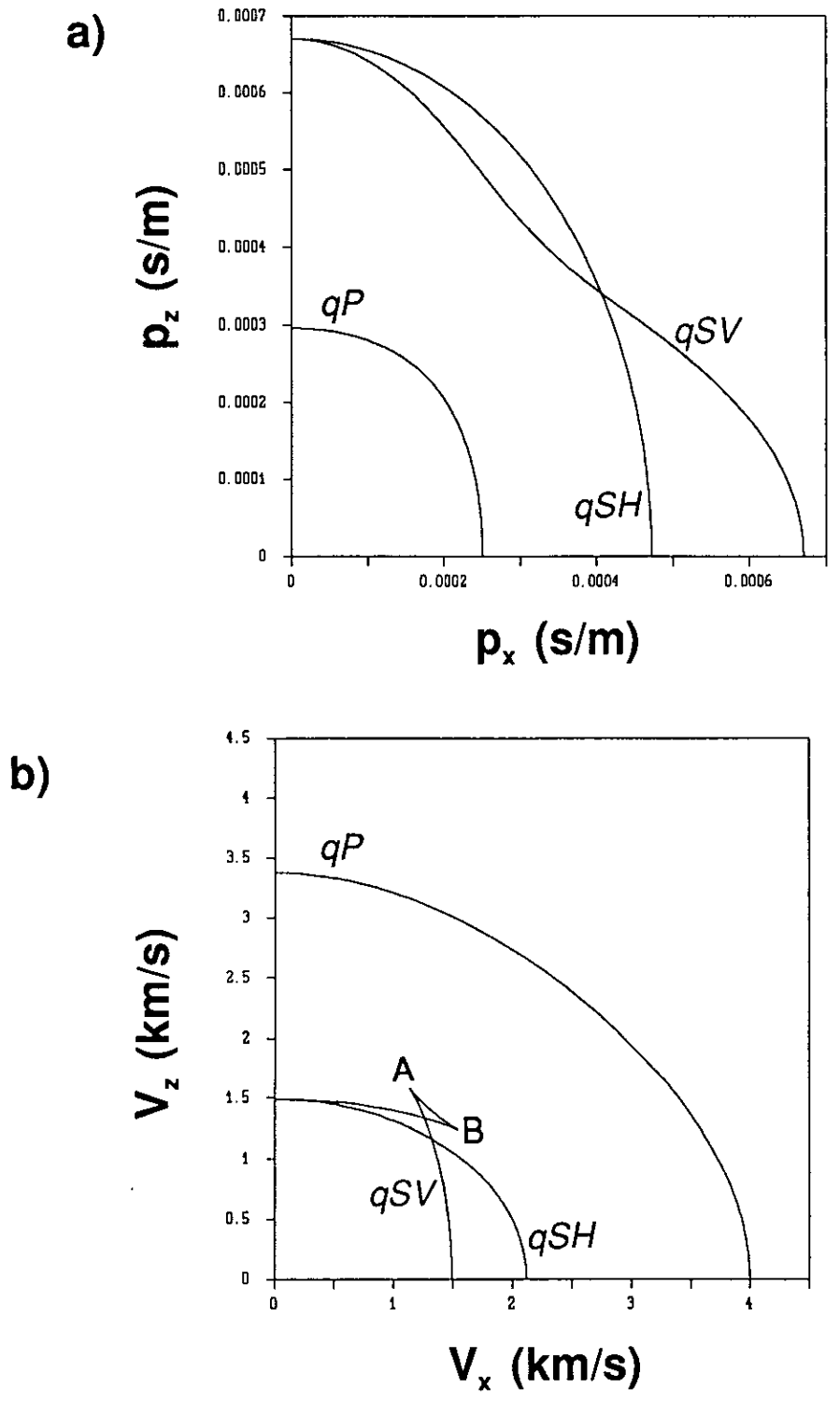

Fig. 10. a) Slowness surface for Williston basin shale. b) Wave surface for Williston basin shale.

2) the anisotropy coefficient for *qSH* waves is 51%. This degree of anisotropy probably exceeds the tolerance of the program due to errors in the calcuation of the direction of the wavefront normal.
Research is continuing in an effort to determine the degree of anisotropy that can accurately be modeled using this algorithm.

The third example involves a model that is both vertically and laterally inhomogeneous in the form of an anticline, and contains an anisotropic layer (Figure 12). The anisotropy parameters (ε, δ and γ) for this layer are identical to the Pierre shale in the previous example. The model velocities vary continuously (ie. there are no layer boundaries where the velocity function has a discontinuous jump), although there is a zone with a strong velocity gradient. The source is positioned near the top of the grid at the crest of the anticline. It is likely that ray tracing through this model would be slow and difficult.

The calculated τ arrays are shown in Figure 13. The first observation to note is that the wavefronts are elongated in the vertical direction, since the velocity generally increases with depth. Close examination of the *qP* and *qSH* wavefronts in Figures 13a and 13c reveals that the wavefront becomes distorted in the anisotropic layer, due to the faster phase velocity in the horizontal direction in this layer. Note that the anisotropic axis is vertical throughout, and does not follow the trend of the anticline. As expected, no distortion of the wavefront is evident for the *qSV* case, since the wave surface here is nearly circular.

Figure 13 provides some indication of the importance of including anisotropy in the forward-modeling calculations. If the model had been completely isotropic, the shape of the *P* and *SH* wavefronts would have resembled the *SV* wavefronts in Figure 13b. The distortion in the wavefront that occurs due to the presence of weak anisotropy implies important differences in the traveltime and the angle of incidence which further complicate other differences in the plane-wave reflection and transmission coefficients (Daley and Hron, 1977).

CONCLUSIONS

A new method has been presented for calculating first arrival traveltimes by solution of the eikonal equation using finite differences. The method is an extension of studies by Vidale (1988) and Qin et al. (1990). Major differences from previous methods are the use of a triangular, rather than a square, grid, and the extension of the method to include transversely isotropic media.

The algorithm discussed here is valid for complex heterogeonous models with moderate to large velocity contrasts, and tracks either head waves or direct arrivals. However, preliminary results suggest that the method is valid for weak anisotropy only, and is not capable of modeling wavefronts that contain cusps. This limitation may not be overly restrictive for sedimentary rocks. Further studies are required to determine the exact range of validity of this technique. Some refinement of the algorithm is planned in order to reduce computation time and to address the problem of systematic error in the calculation of the direction of the wavefront normal, due to the assumption that the wavefront is locally planar. Another planned refinement is the calculation of geometrical spreading along with the traveltime.

FIG. 11. (next page) a) *qP*-wave traveltime array calculated for Pierre shale. Compare to wave surface (Figure 10b). The wavefronts, represented by the boundaries between different shades, are approximately elliptical in shape. The tendency of the wavefronts to assume a hexagonal appearance is an artifact of the grid geometry, and is likely due to a sysmtematic error in estimating the direction of the wavefront normal. The wavefront is assumed to be locally planar. b) *qSV*-wave traveltime array for Pierre shale. The wavefronts are approximately circular, as expected from the theoretical wave surface (Figure 10b). c) *qSH*-wave traveltime array for Pierre shale.

FIG. 12. (page after next) a) Vertical *qP*-wave phase velocity (α_0) for anticline model. The velocity function is continuous and monotonically increasing with depth, with a high gradient zone at an intermediate level. The source position is indicated by the dot. b) Vertical *qS*-wave velocity (β_0) for anticline model. c) Anisotropic zone in anticline model (shaded area), just above high velocity-gradient zone. Anisotropy parameters are the same as the Pierre shale: $\varepsilon = 0.11$, $\delta = 0.09$, $\gamma = 0.165$.

FIG. 13. (two pages after next) a) Calculated *P*-wave traveltimes for anticline model. The wavefront is generally elongated in the vertical direction due to the velocity increase with depth. Note also the distortion of the wavefron in the anisotropic zone on the flanks of the anticline. b) Calculated *qSV*-wave traveltimes for anticline model. Wavefront distortion in the anisotropic zone is very slight. c) Calculated *qSH*-wave traveltimes for anticline model.

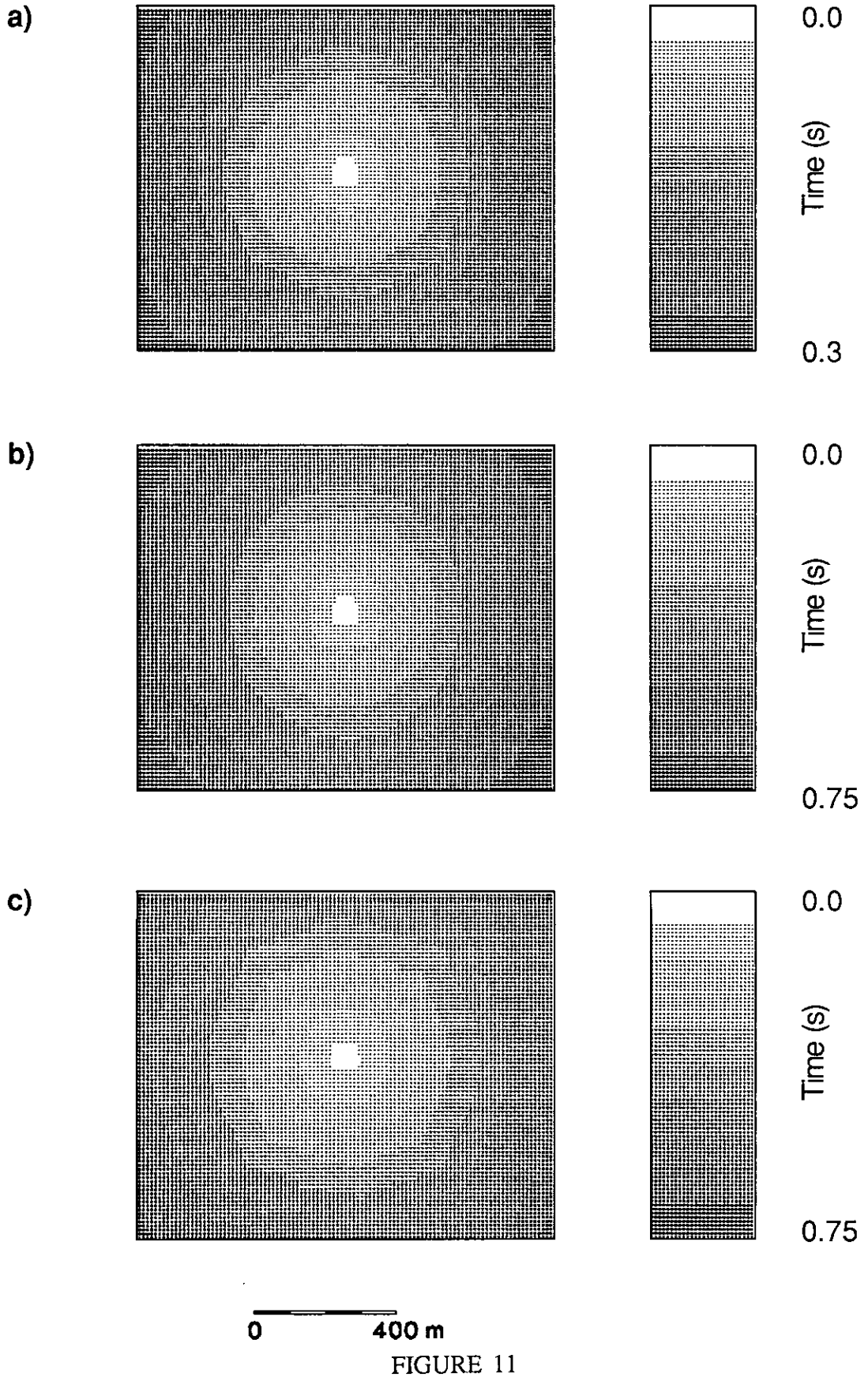

FIGURE 11

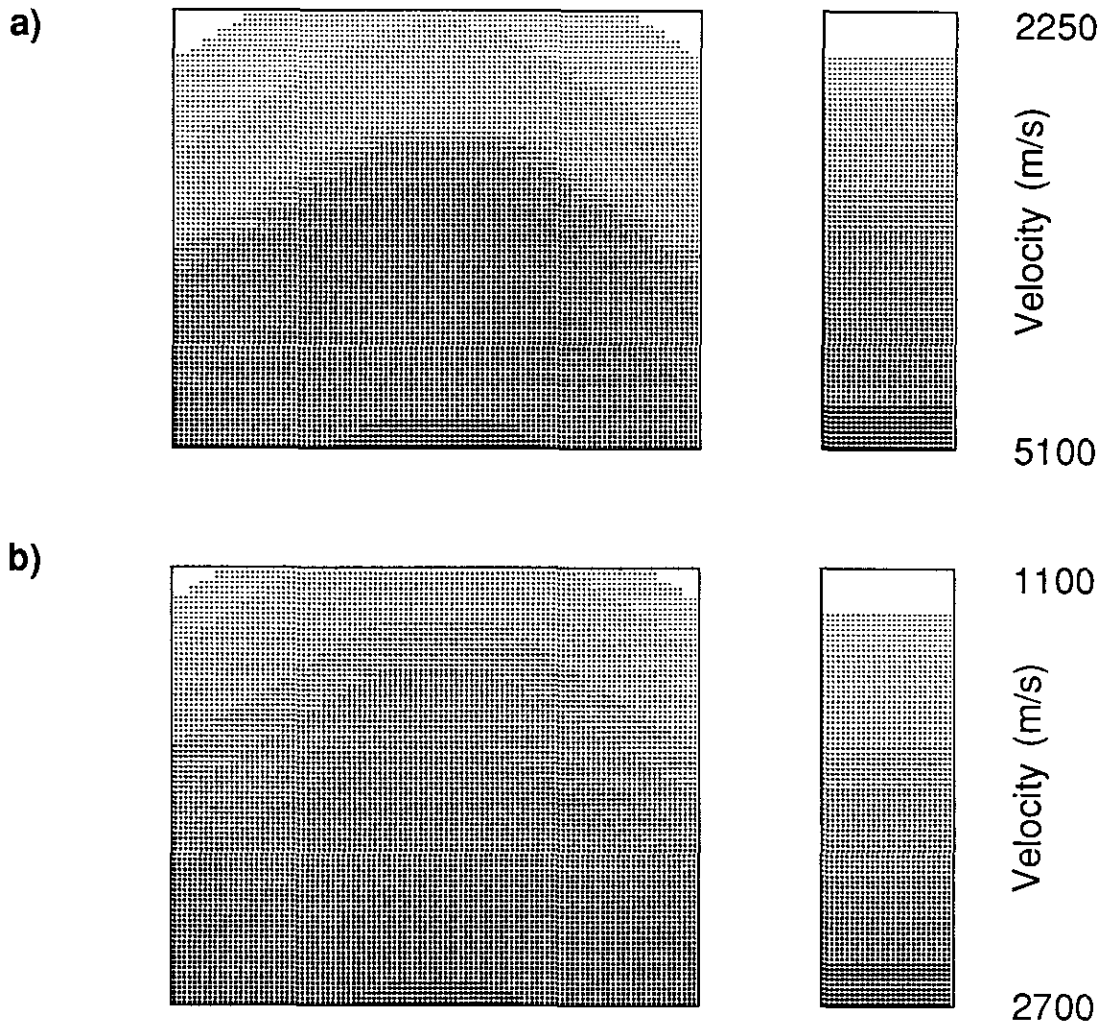

FIGURE 12

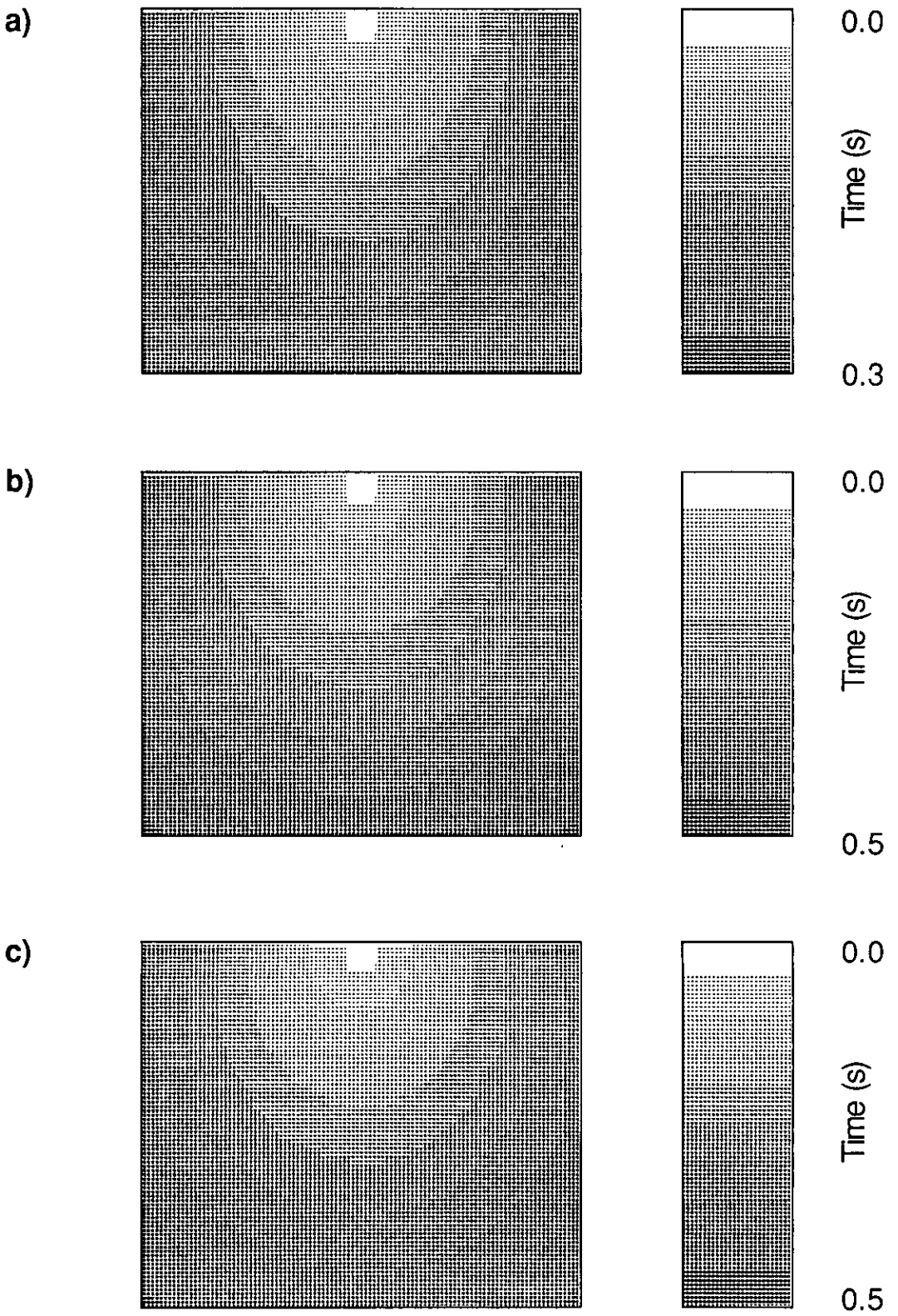

FIGURE 13

ACKNOWLEDGMENTS

I would like to thank Don Easley, who suggested the use of a triangular grid and provided many other helpful suggestions, as well as my supervisor, Dr. Robert R. Stewart. I am also grateful for the financial support of the sponsors of the CREWES project at the University of Calgary.

REFERENCES

Bleistein, N., 1984, Mathematical methods for wave phenomena: Acedemic Press.

Cerveny, V., Molotkov, I.A., and Psencik, I., 1977, Ray method in seismology: Univerzita Karlova, Prague.

Crampin, S., Chesnokov, E.M., and Hipkin, R.A., 1984, Seismic anisotropy--the state of the art: Geophys. J. Roy. Astr. Soc., 76, 1-16.

Daley, P.F., and Hron, F., 1977, Reflection and transmission coefficients for transversely isotropic media: Bull., Seis. Soc. Am., 67, 661-675.

Jones, E.A., and Wang, H.F., 1981, Ultrasonic velocities in Cretaceous shales from the Williston basin: Geophysics, 46, 288-297.

Kendall, J-M., and Thomson, C.J., 1989, A comment on the form of the geometrical spereading equations, with some numerical examples of seismic ray tracing in inhomogeneous, anisotropic media: Geophys. J. Int., 99, 401-413.

Musgrave, M.J.P., 1970, Crystal Acoustics: Introduction to the study of elastic waves and vibrations in crystals: Holden-Day.

Qin, F., Olsen, K.B., Luo, Y., and Schuster, G.T., 1990, Solution of the eikonal equation by a finite-difference method. Presented at the SEG 60th Ann. Intl. Mtg., San Francisco, Expanded Abstracts 1004-1007.

Rothman, D.H., 1988, Cellular-automaton fluids: A model for flow in porous media: Geophysics, 53, 509-518.

Singh, S.C., and Chapman, C.H., 1988, WKBJ seismogram theory in anisotropic media: J. Acoust. Soc. Am., 84, 732-741.

Thomsen, L., 1986, Weak elastic anisotropy: Geophysics, 51, 1954-1966.

Vidale, J., 1988, Finite-difference calculation of travel times: Bull., Seis. Soc. Am., 78, 2062-2076.

Vlaar, N.J., 1968, Ray theory for an anisotropic inhomogeneous elastic medium: Bull., Seis. Soc. Am., 58, 2053-2072.

White, J.E., Martinequ-Nicoletis, I., and Monash, C., 1982, Measured anisotropy in Peirre shale: Geophys. Prosp., 31, 709-725.

APPENDIX
Basic ray theory for inhomogeneous, anisotropic elastic media

A brief introduction to ray theory for inhomogenous, anisotropic elastic media is presented here. For further detail, the reader is referred to Vlaar (1968), Cerveny et

al. (1977) and Kendall and Thomson (1989). The equations of motion are derived from generalized Newton's law and generalized Hooke's law. In the absence of sources, the frequency-domain equations of motion are

$$(c_{ijkl}u_{k,l})_{,j} + \omega^2\rho u_i = 0 \ , \tag{A-1}$$

where c_{ijkl} is the 81-component elastic stiffness tensor with symmetry properties $c_{ijkl} = c_{jikl} = c_{ijlk} = c_{klij}$, u_i is the *ith* component of displacement, ρ is density, Einstein's summation convention for repeated indices is used and a comma implies spatial differentiation. In the ray method, a solution is sought in the form of an asymptotic series

$$u_k(\mathbf{x},\omega) = \sum_{n=0}^{\infty} \frac{U_k^{(n)}(\mathbf{x})}{(-i\omega)^n} e^{i\omega\tau(\mathbf{x})} \ . \tag{A-2}$$

Substitution of (A-2) into (A-1) leads to a new system of differential equations (Cerveny et al., 1977), all of which are set to zero. A high frequency approximation is obtained by setting the coefficient of ω^2 to zero:

$$c_{ijkl}U_k^{(0)}p_ip_l - \rho U_j^{(0)} = 0 \ . \tag{A-3}$$

A non-trivial solution to (A-3) requires that

$$det|p_ip_lc_{ijkl} - \rho\delta_{jk}| = 0 \ , \tag{A-4}$$

where $p_i = \partial\tau/\partial x_i$ is the slowness vector. Equation (A-4) may be regarded as a nonlinear first-order differential equation for the wavefront, or *eikonal*, τ, and thus is the equivalent to equation (1) for the isotropic case. Multiplying (A-4) by v^2, where v is the phase velocity, leads to the Kelvin Christoffel equation

$$det|\Gamma_{jk} - \rho v^2\delta_{jk}| = 0 \ , \tag{A-5}$$

where $\Gamma_{jk} = n_in_lc_{ijkl}$ and n_i is the unit vector normal to the wavefront.